mater.scichina.com link.springer.com

Published online 4 November 2022 | https://doi.org/10.1007/s40843-022-2221-y
Sci China Mater 2023, 66(3): 1132–1139

Topological defects and their induced metallicity in monolayer semiconducting γ-phase group IV monochalcogenides

Shengfeng Zeng and Xiaolong Zou*

ABSTRACT **γ-Phase group IV monochalcogenides (γ-MX), predicted to be stable with semiconducting characteristics, have been synthesized by chemical vapor deposition but showing metallicity. The ubiquitous topological defects introduced during the growth process could bring about key influences on the electronic behaviors, but their structures and properties remain unexplored. Taking monolayer γ-GeSe as an example, first-principles calculations were performed to investigate the structural, thermodynamic, and electronic properties of dislocation cores (DCs) and grain boundaries (GBs). Various derivative DCs emerge depending on different arrangements of atoms. The calculated low-energy DCs are then used to determine preferential structures of GBs *versus* tilt angle, with special attention paid to the whole family of 60° twin GBs, showing distinct hexagons or Ge–Ge bonds. Furthermore, electronic structures are calculated for thermodynamically favored 21.8° with closely packed dislocations and 60° twin GBs. Most of them show a strong resonance between the bulk and dislocation states, rendering the systems metallic, while some display semiconducting behaviors with reduced band gap. These electronic properties are universal for other γ-MXs. The simulated scanning tunneling microscopy images show characteristic fingerprints to help identify their existence in practice. Our results show that topological defects in γ-MX with versatile properties should be carefully engineered for their potential applications.**

Keywords: 2D materials, group IV monochalcogenides, dislocations, grain boundaries, first-principles calculations

INTRODUCTION

Two-dimensional (2D) materials have attracted much research interest, because of their vast potential applications including electronics, opto-electronics, catalysis, and energy storage and conversion [1–8]. A rising star of 2D materials is group IV monochalcogenides (MX), which show fascinating properties, including high-temperature coupled ferroelectricity and ferroelasticity, giant piezoelectricity, photostriction, switchable charge and spin photogalvanic effects, high-performance thermoelectricity, and persistent spin helix behaviors [9–25]. Recently, a new phase of group IV MX, γ-MX, has been theoretically predicted with the energy more favorable than common α and β phases especially in thin-film limit [26], thanks to the M-M interaction in thin layers. Interestingly, γ-MX exhibits stacking-dependent polarization and spin splitting [27], high electron mobility, as well as a camel's back-like band structure, which leads to unique high-temperature electron-hole liquid states [26]. Soon after the prediction, one of the γ-MX, i.e., γ-GeSe, was synthesized through chemical vapor deposition (CVD) on Au-coated SiO_2/Si wafers, but exhibiting metallicity rather than predicted semiconducting behaviors of the pristine structure [28], which highlights the crucial influences of defects. Inevitably, various structural defects with different dimensionalities and topologies can be introduced during the CVD process. In particular, topological defects including dislocation cores (DCs) and grain boundaries (GBs) arise naturally when crystal grains with different orientations merge. Having different arrangements of atoms from their pristine structure, topological defects in 2D materials can bring about unique electronic, magnetic, catalytic, and optical properties [29–37], for instance, conducting twin GBs along the periodic direction in otherwise semiconducting transition metal dichalcogenides (TMDs) [29,38] and environment-controlled superplasticity [39]. Despite the significance of topological defects in determining the properties and applications of monolayer γ-MX, the related study is absent. Not only do the atomic arrangements of DCs and GBs require to be determined, but their impacts on material properties should be explored for purposeful defect engineering towards potential applications.

Taking monolayer γ-GeSe as an example, we systematically investigate the structural, thermodynamic, and electronic properties of its DCs and GBs using the first-principles calculations with details provided in the Supplementary information. Due to the close proximity of Ge and Se in the periodic table and the four-layer arrangement of atoms in monolayer γ-GeSe, various DCs emerge, depending on how different atoms are arranged in the DCs, significantly different from 1H-TMDs and h-BN cases. Based on the obtained low-energy DCs, GBs with different tilt angles, along with a rich family of 60° twin GBs, are constructed and further explored for the energy variability and electronic properties as well. Interestingly, most of them exhibit a strong resonance between the bulk and dislocation states leading to metallic features, whereas some show semiconducting behaviors with dispersive defect states and greatly reduced band gap. These electronic properties are universal for other γ-MXs. The simulated scanning tunneling microscopy (STM) images indicate that thermodynamically favored GBs exhibit distinct

Shenzhen Geim Graphene Center, Tsinghua-Berkeley Shenzhen Institute and Tsinghua Shenzhen International Graduate School, Tsinghua University, Shenzhen 518055, China
* Corresponding author (email: xlzou@sz.tsinghua.edu.cn)

features under both positive and negative bias voltages. These topological defects with distinct properties offer new prospects for engineering towards purposeful applications.

EXPERIMENTAL SECTION

First-principles calculations

All first-principles density functional theory calculations were carried out by using the projector-augmented wave [40] potentials for ion-electron interaction in the framework of Vienna *Ab-initio* Simulation Package [41]. Generalized gradient approximation [42] for Pendew-Burke-Ernzerhof functional [43] was adopted to describe the exchange-correlation interaction. The energy cutoff for plane-wave basis was set to 400 eV. The Monkhorst-Pack *k*-point sampling was applied, with grid sizes of ~0.2 $Å^{-1}$. Based on periodic boundary conditions (PBC), a vacuum layer larger than 10 Å was chosen along the out-of-plane direction. All structures were fully optimized until the energy and force were converged to 1×10^{-5} eV and 0.01 eV $Å^{-1}$, respectively. Nanoribbon models were constructed for determining stable DCs, while PBC models with a distance of ~20 Å between two GBs were built for GB energy and electronic properties. GB energies were calculated as $E_{GB} = (E_{total} - \sum_i n_i\mu_i)/2$, with E_{total}, n_j, and μ_i representing the total energy of PBC models containing two equivalent GBs, the number of Ge or Se atoms in the supercell, and their corresponding chemical potentials. The thermodynamic equilibrium condition $\mu_{GeSe} = \mu_{Ge} + \mu_{Ge}$ was adopted, with μ_{GeSe} being chemical potential of a GeSe unit in pristine γ-GeSe. The STM images were simulated based on the Tersoff-Hamann approach [44], in which the tunneling current is proportional to the local density of states (DOS) around the Fermi level, with the distance between the tip and the surface of γ-GeSe set at 2 Å. The visualization of STM images was performed by VESTA [45].

RESULTS AND DISCUSSION

Structures and thermodynamic energies of DCs

Fig. 1a displays the atomic structure of monolayer γ-GeSe, which shows a four-layer Se-Ge-Ge-Se configuration, possessing an A-B-C-A stacking sequence. Distinct from α- and β-phase MXs with an orthorhombic lattice, monolayer γ-GeSe belongs to the $P\bar{3}m1$ space group with a hexagonal crystal lattice, which makes it feasible to construct DCs of γ-GeSe in the same way as adopted in monolayer TMD cases, by removing a half-line of atoms (shaded area in Fig. 1b) [29]. The resulting DCs are characterized by the topological invariant named Burgers vector $\boldsymbol{b}$, which is the topological mismatch for an arbitrarily closed contour encircling dislocations. Since the dislocation energy is proportional to $\boldsymbol{b}^2$, we focus on DCs with the smallest $\boldsymbol{b}$, i.e., (1, 0) and (0, 1). Depending on different termination species of the removed half-line of atoms, six different types of DCs emerge with square-hexagon 4|6, pentagon-heptagon 5|7, and hexagon-octagon 6|8 rings, named as I–VI shown in the lower panels of Fig. 1b. Due to the inversion symmetry of monolayer γ-GeSe, these DCs can transform into each other by adding (or removing) different amounts of Ge or Se atoms, indicated by the arrows between neighboring panels. To make our presentation clear, these DCs are artificially classified into two groups according to the arrangement of atoms at the top vertices of these cores, i.e., Se-(I–III) and Ge-oriented (IV–VI) ones.

Different DCs exhibit different kinds of polygons and different numbers of atoms at the hollow sites of polygons, which can induce a significant level of strains at the cores, thus bringing about an effective interaction between DCs and point defects. Because of the specific A-B-C-A stacking, DCs in γ-GeSe have much richer variety compared with the 1H-MoS_2 case. Here, we only consider the interaction between DCs and Ge/Se vacancies or interstitials for simplicity, and the obtained derivative dislocations are displayed in Fig. 2a. For Se-oriented DCs, there are eight different DCs after considering the dislocation-point defect interaction, as shown in the top two panels. Four DCs share the 4|6 shape, which can be converted into the other four in 5|7 topology by the adsorption of a pair of Se interstitials. Similarly, for Ge-oriented DCs, there are twelve different DCs having 4|6, 5|7, or 6|8 shape, and they can transform into each other by adding/removing one Ge or a pair of Se atoms, indicated by the arrows in the bottom three panels. Further, by choosing different core configurations, it can be seen that Se-oriented DC-III and Ge-oriented DC-III' are equivalent, highlighting the influences of inversion symmetry (more details are shown in Fig. S1). Accordingly, the relative energies for all DCs can be calculated as $E = E_{der} - E_{ref} - \sum_i n_i\mu_i$, where E_{der}, E_{ref}, and n_i are the energy of

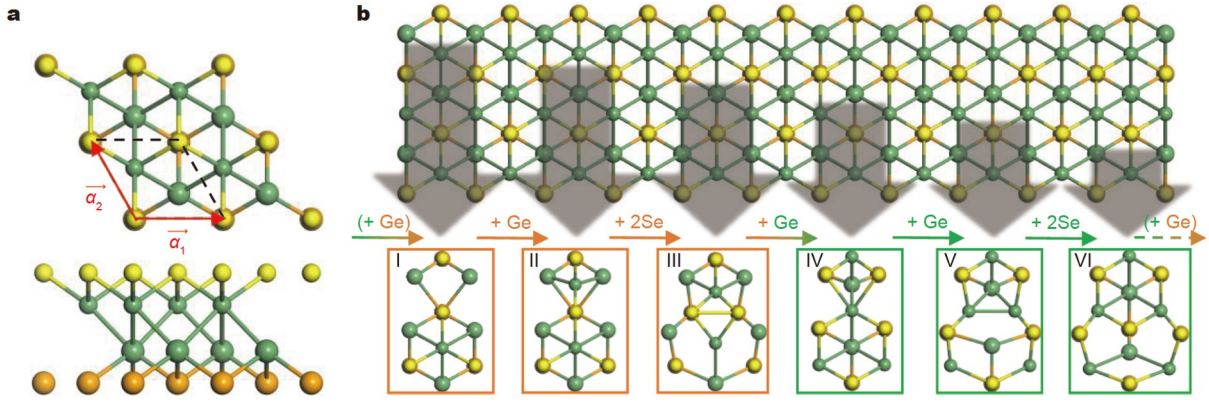

Figure 1 (a) Atomic structure of monolayer γ-GeSe, in a four-layer Se-Ge-Ge-Se configuration, with Ge in green and Se in yellow (top) or orange (bottom). Atoms in different layers are represented by spheres of different sizes. (b) Schematic for the construction of Se- and Ge-oriented DCs by removing half-line of atoms with different termination species, as indicated by shaded areas.

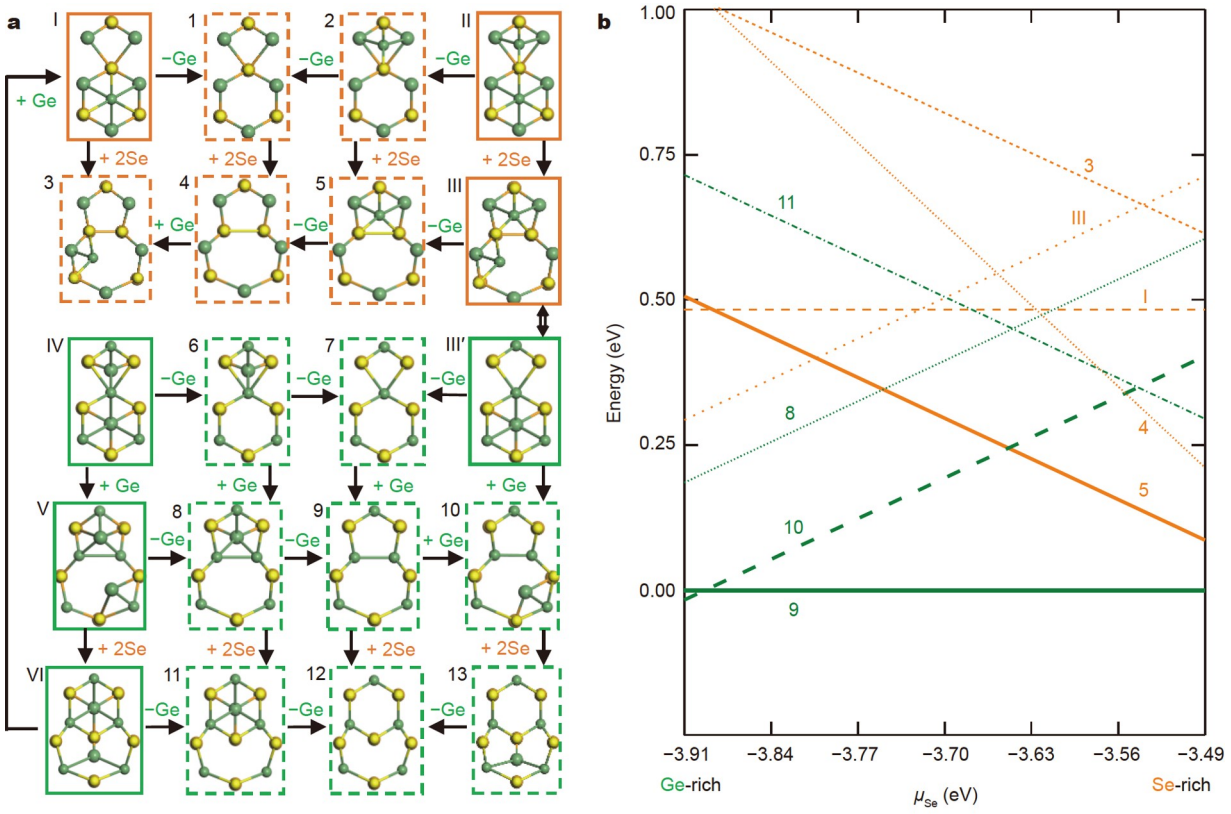

Figure 2 (a) Derivative DCs obtained by interacting with Ge/Se vacancies or interstitials, with Se- and Ge-oriented DCs in orange and green panels, respectively. (b) Relative energies of DCs as a function of Se chemical potential.

a derived dislocation, the energy for the reference dislocation, and the number of added atoms in the derived structure. Here, μ_i is the corresponding chemical potential satisfying the thermodynamic equilibrium condition $\mu_{GeSe} = \mu_{Ge} + \mu_{Se}$, with μ_{GeSe} being the chemical potential of pristine γ-GeSe in a unit cell. Fig. 2b plots the dislocation energies for some low-energy DCs *versus* μ_{Se} with DC-9 as the reference, while results for all DCs are shown in Fig. S2.

It can be seen that all low-energy DCs exhibit 5|7 topology, with either 0 or 1 Ge atom at the center of polygons. For Ge-oriented cases, DC-9 with empty 5- and 7-membered rings as well as shared Ge-Ge bonds in the center of 5|7 is the lowest in energy. When one additional Ge is introduced to the heptagon of DC-9 to form DC-10, the heptagon is too large for a single Ge, so that it will shift off the symmetric central line of the dislocation to bond with Se atoms on one side after structural relaxation. The reconstruction leaves the added Ge atom not fully saturated, leading to a higher energy of DC-10. For DC-8, the additional Ge atom is located at the center of the much smaller pentagon, which leads to an increase of strain energy and the formation of more unfavorable homoelemental Ge–Ge bonds (compared with heteroelemental Ge–Se bonds), thus giving rise to higher dislocation energy than DC-10. For Se-oriented DCs with Se–Se bonds in the center, the addition of one Ge atom at the center of the pentagon in DC-5 results in the formation of three preferred heteroelemental Ge–Se bonds, giving rise to its more favorable energy compared with DC-3 and DC-4. Nevertheless, these DCs have generally low relative energies, smaller than 1 eV in almost all the range of μ_{Se}, and consequently, they will dominate in synthesized polycrystalline samples.

Evolution of structures and energies of GBs *versus* tilt angle *α*

An array of the dislocations can be used to construct GBs, characterized by the tilt angle α and specific dislocation configurations. Here, the low-energy Ge-oriented DC-9 and Se-oriented DC-5 in Fig. 2a are chosen. Because of the PBC adopted in the calculations, it is convenient to restrict our discussion to bisecting GBs with the GB line along the angular bisector of the tilt angle α between two grains. Bisecting GBs for hexagonal γ-GeSe can be constructed by rotating two grains apart along either armchair (A) or zigzag (Z) direction, as indicated by the green and orange lines in the central panel of Fig. 3, with resulting structures categorized as A-GBs and Z-GBs, respectively. Due to its C_3 symmetry, the pristine structure can be recovered when α reaches 120°. Configurations in the ranges from 0° to 60° and from 60° to 120° are identical but with opposite orientations, as shown in left and right panels of Fig. 3 for Z- and A-GBs, respectively. It is known that for structures without inversion symmetry such as 1H-MoS_2 and h-BN, A-GBs and Z-GBs are different in terms of their mirror symmetry with respect to the GB line [29,46]. Although γ-GeSe exhibits inversion symmetry, its specific A-B-C-A stacking renders A- and Z-GBs nonequivalent, as detailed below.

Starting from the A direction, GBs emerge as sparsely distributed dislocations with mirror symmetry along the GB line, and the density of dislocation grows with increasing α. Once α is larger than 32.2°, GBs are constituted by a series of tilted DCs

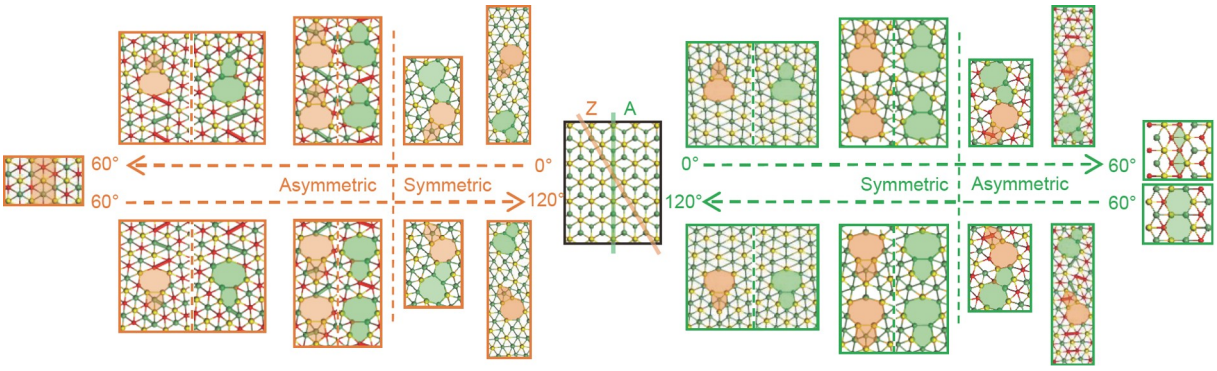

Figure 3 Tilt-angle-dependent configurations of Z- (left) and A-GBs (right), which result from the rotation of two grains with respect to zigzag and armchair directions (orange and green lines in the central panel, respectively). Both Z- and A-GBs could have symmetric and asymmetric structures. For asymmetric GBs, Ge atoms in different atomic layers are distinguished by red and green, with corresponding horizontal Ge–Ge bonds highlighted as sticks in the models.

without mirror symmetry. For these asymmetric large-angle GBs, Ge atoms on two sides of dislocations are located in different atomic layers (i.e., B and C layer in A-B-C-A stacking), which are inversion symmetrically related to each other, as indicated by red and green spheres in Fig. 3. A more detailed analysis is provided in Fig. S3. Along with the formation of asymmetric GBs, Ge–Ge bonds formed by Ge atoms in the same atomic layer emerge, highlighted as red or green sticks in the right panels. These Ge–Ge bonds are named as horizontal Ge–Ge bonds hereafter. As α becomes larger, the number of such horizontal Ge–Ge bonds increases. Similarly, starting from the Z direction, sparsely distributed and tilted dislocations with mirror symmetry emerge, and become closely packed when α reaches 27.8°. As α continues to increase, the dislocations turn to asymmetric with horizontal Ge–Ge bonds formed along GBs.

After illustrating the structural evolution of GBs, their energies per unit length *versus* α can be feasibly calculated, which are also chemical-potential-dependent. Although the stability of defective systems can be measured by a (p, T) diagram under an equilibrium condition [47,48], the formation of GBs and topological dislocations is a non-equilibrium process, depending on the tilt angle preset by the growth history [29,49]. A more relevant process is the reconstruction of DCs under certain tilt angles as discussed above, so we focus on the relative stability of different GBs. Considering the fact that the boiling point of Se (958 K) is much lower than that of Ge (3106 K), the Se-rich condition can be readily achieved in experiments. Here, GB energies under Se-rich conditions are shown in Fig. 4, with α either from A or Z direction represented by the bottom green or top orange axis, respectively, while the results under Ge-rich conditions are displayed in Fig. S4. For A-GBs, GB energy first increases with α slowly, in line with the growing dislocation density as α increases. When α reaches 32.2°, GB energy experiences a notable increase, owing to the significant strain induced by the asymmetric arrangement of atoms around GBs, which brings about severe structural reconstructions, as shown in Fig. S5. For GBs with even larger α, their energies are determined by the balance between the strain energy and chemical energy of horizontal Ge–Ge bonds. Notably, 60° twin A-GBs possess much lower energies compared with other large-angle ones, and their structural evolution and energies will be discussed in detail later. For Z-GBs, a similar trend of energy *versus* α is observed, with the energies for small-angle GBs slightly higher than those of small-tilt A-GBs.

Construction of a full set of 60° twin GBs and their thermodynamic stability

It should be emphasized that for γ-GeSe with both C_3 and inversion symmetry, the 60° tilt cannot restore its perfect lattice as the graphene case, because of its four-layer stacking structure. Due to their thermodynamically favorable characteristic, 60° GBs are expected to be dominant in polycrystalline samples with large-angle tilts, similar to TMDs [29]. Following a similar strategy applied in TMDs [50], all possible 60° GBs configurations are searched. As schematically shown in Fig. 5a, starting from a specific 60° GB consisting of a row of Se–Se bonds with a Ge atom located at each hollow site, named as GB-1, one could build GB-2 and GB-7 by removing a line of Ge and two Se atoms, respectively. The two resulting GB structures are equivalent to setting the growth front of the left grain as Se- or Ge-terminated, respectively. Then, all 60° GBs can be constructed based on GB-2 and GB-7 by alternatively removing a line of Ge, Ge, and two Se atoms, indicated by the arrows between neighboring panels in Fig. 5a. The closed loop of the structural evolution formed by sequentially removing a line of atoms guarantees that all 60° GBs have been obtained. It is noteworthy that GB-1 and GB-4 appear twice, highlighting the influences of inversion symmetry, different from TMD cases. Among all these structures, GB-3 and GB-8 have the same number of Ge–Se bonds as the pristine lattice, with slight differences resulting from the misplaced Ge atoms. Ge atoms along GB-8 are all located in the top Ge stacking layer, forming a zigzag horizontal Ge–Ge line, while along GB-3 horizontal Ge–Ge bonds emerge along the A direction in the bottom Ge stacking layer. Meanwhile, GB-2, 4, and 10 are composed of hexagons with Se–Se, Se–Ge, and horizontal Ge–Ge bonds along the GBs, respectively.

With all 60° GBs obtained, Fig. 5b plots the relative energies of some low-energy configurations as functions of μ_{Se} taking GB-1 as the reference, while some high-energy ones containing homoelemental Se–Se bonds are not shown. It can be observed that energies of these 60° GBs are close to each other, except for those with abundant Ge atoms along GBs, such as GB-7. In particular, among the three structures with the lowest energies, the energy of GB-8 is only slightly lower than that of GB-10 by 0.003 eV Å^{-1}, while GB-4 exhibits the lowest energy under

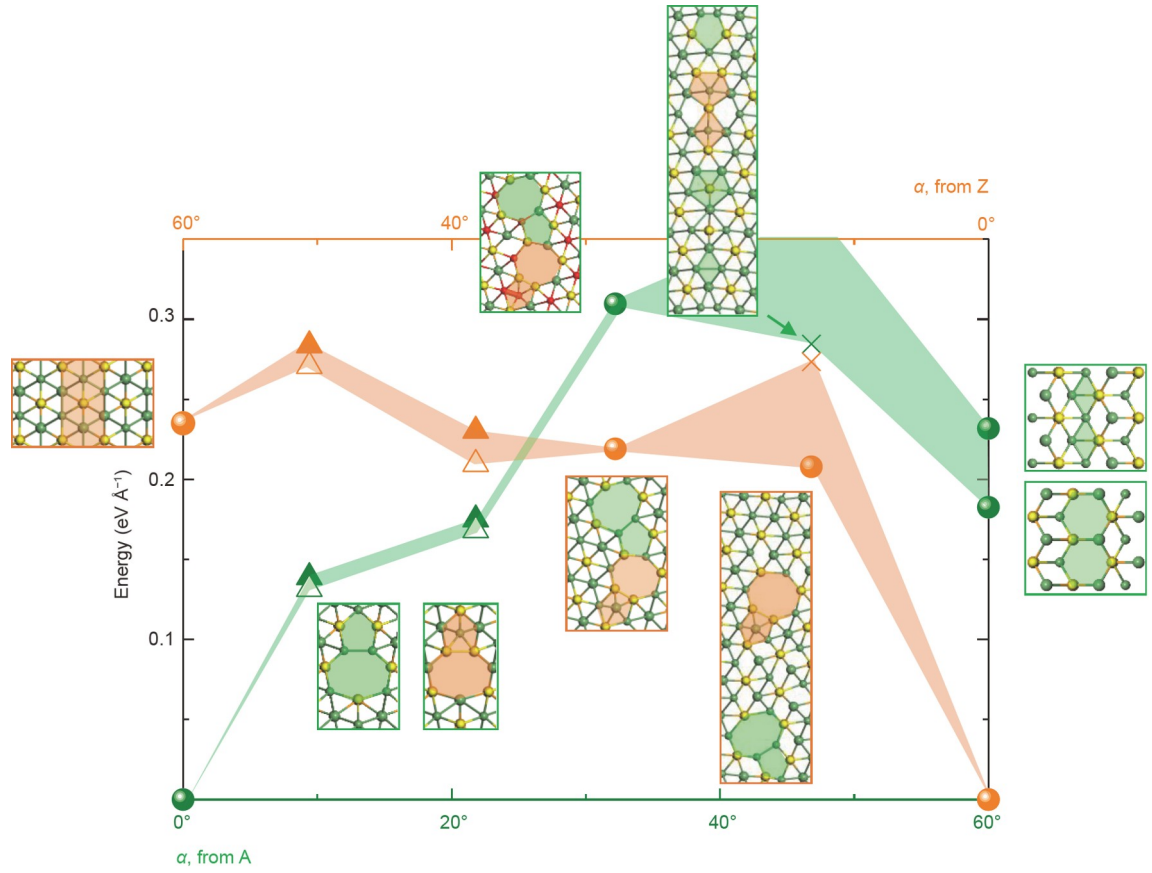

Figure 4 GB energies either from armchair direction (bottom green axis) or from zigzag direction (top orange axis). Shaded areas denote energy ranges for considered GBs. Solid and empty triangles are for GBs containing only Ge-oriented 5|7 and Se-oriented 5|7, respectively. Solid circles are for GBs with alternating Ge- and Se-oriented 5|7, and crosses are for symmetric GBs consisting of pentagons and rhombs.

Se-rich conditions in comparison with GB-8 and GB-10. These results indicate that filled hexagons with the same heteroelemental coordination as the pristine lattice and empty hexagons with misplaced Ge–Ge bonds or heteroelemental Ge–Se bonds are favorable structural units in 60° GBs.

Induced metallicity in low-energy GBs

The topological defects can significantly influence electronic properties of materials, as shown in graphene and TMDs [29,50,51]. Here, we consider the electronic structures for two 21.8° A-GBs (composed of either Ge-oriented DC-9 or Se-oriented DC-5) and three lowest-energy 60° GBs (GB-4, 8, and 10). Their band structures and DOS are plotted in Fig. 6 with the projected contributions from dislocations/GBs represented by blue circles and red lines. For 21.8° A-GBs, both structures have two defect levels inside the original bulk gap and show intriguing metallicity with the Fermi level crossing dispersive bands. The metallicity is closely related to the formation of defect states inside the bulk valence bands, leading to a resonance between the defect and bulk states. For Ge-oriented GB in Fig. 6a, these resonance defect states lie deep in the range of [−1, −0.25] eV, while the original gap keeps intact with the same gap size of 0.6 eV as the pristine lattice. Distinctly, some defect states of Se-oriented GB in Fig. 6b move to the top of valence bands and are intersected by the Fermi level, which reduces the gap to around 0.4 eV. Different from other 2D materials, the emergence of metallicity in small-angle GBs for γ-GeSe is related to the close electronegativity between M and X atoms. Specially, for inversion GBs in TMDs, early theoretical simulations [29] indeed predicted the metallicity states for the GBs, which is attributed to the polar discontinuity across the boundaries [38]. STM provides direct evidence for such 1D metallic states, which further gives rise to characteristic charge density wave states and spin-charge separation [52,53]. However, the observation of metallicity in γ-MX and its consequences on the GB properties require further investigation. More discussion on the metallicity of GBs in different 2D materials is provided in Fig. S6.

In contrast, three considered 60° GBs with the smallest periodicity along GBs exhibit diverse electronic properties, despite the common features of the camel's back at the valence bands top as the pristine case [26]. For GB-4 composed of hexagons with heteroelemental Se–Ge bonds, Fig. 6c shows similar deep resonance states and metallicity as 21.8° GB cases. However, the bands near the Fermi level exhibit stronger dispersion compared with small-angle ones, attributed to larger wavefunction overlap among the densely packed empty hexagons. Differently, GB-8 and GB-10 with horizontal Ge–Ge bonds along Z and A directions show semiconducting behaviors, with more dispersive defect states appearing at the bottom of conduction bands or inside the pristine band gap, which greatly reduce the band gap to 0.25 and 0.2 eV, respectively. Top panels of Fig. 6 also plot the local DOS for atoms around GBs as indicated by the shadow area in the middle panels of Fig. 6. It can be seen that these atoms only contribute partially to the total DOS, in particular for

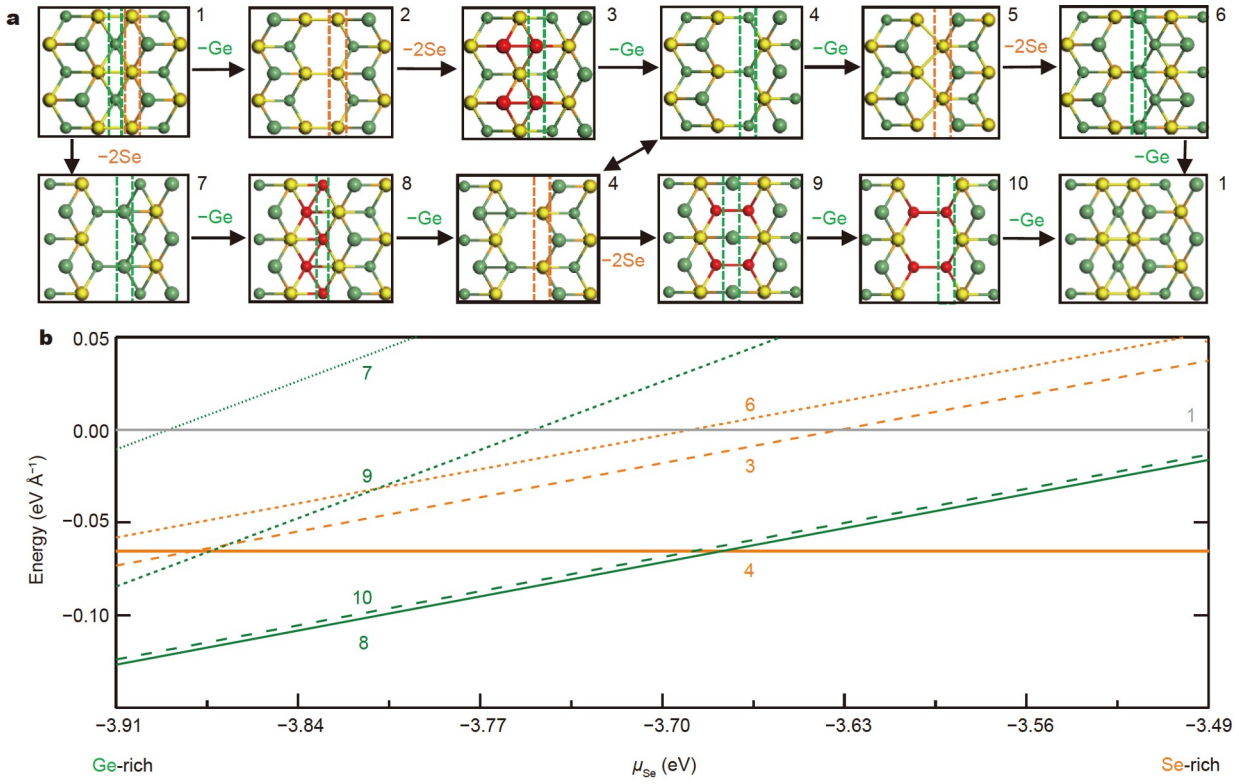

Figure 5 (a) Construction of all possible 60° GBs by removing a line of Ge or two Se vacancies sequentially. The horizontal Ge–Ge bonds are highlighted in red. (b) Relative energies of 60° GBs *versus* chemical potentials of Se.

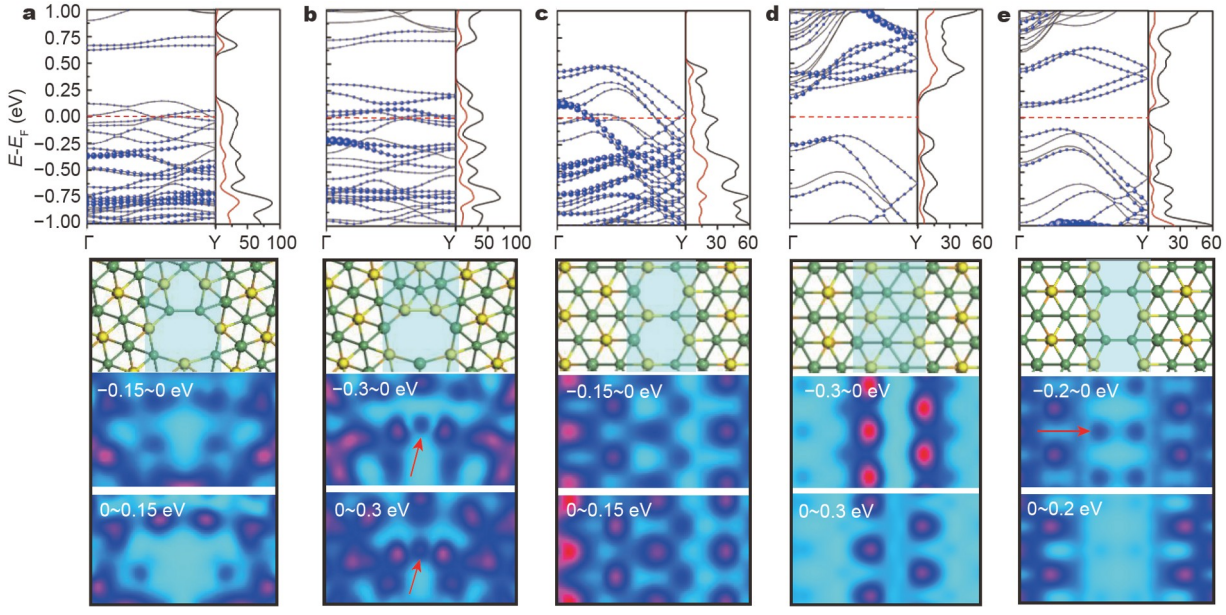

Figure 6 Band structures and DOS for (a) 21.8° Ge-oriented and (b) 21.8° Se-oriented GBs, as well as three 60° GBs, i.e., (c) GB-4, (d) GB-8, and (e) GB-10, with projected contributions from atoms around DCs represented by blue circles and red lines. Their atomic GB configurations and simulated STM images are displayed below, with GBs in shaded areas and bias voltage ranges specified in each panel.

metallic 21.8° GBs and 60° GB-4, which indicates the important contribution from bulk states, a key feature of resonance effect. It is worthy to point out that the resonance-induced metallicity could contribute to the experimentally observed high conductivity.

The GB structures and properties of GeS, SnS and SnSe were further investigated, as shown in Fig. S7. It can be seen that they show similar characteristics as the GeSe case. The 21.8° GBs and 60° GB-4 exhibit the same resonance effects between defect and bulk states with defect states deep in the valence bands, leading

to metallic features. Whereas, 60° GB-8 and GB-10 show reduced band gaps compared with pristine materials, i.e., 0.4 and 0.2 eV for the GeS case, 0.5 and 0.4 eV for the SnS case, 0.4 and 0.15 eV for the SnSe case, respectively. These results clearly show the universal metallicity of GBs in γ-MX, which is related to the resonance effect induced by the close electronegativity between M and X atoms.

Different GBs with distinctive metallicity or reduced band gap can be identified by STM, where the tunneling current between the tip and samples provides unique structural fingerprints. The bottom panels in Fig. 6a–e show the simulated STM images for each GB, considering both electron and hole tunneling cases by applying positive and negative bias voltages in different ranges as specified in each panel. The detailed correspondence between STM images and atomic structures is shown in Fig. S8. For two 21.8° GBs, current intensities of both Ge- and Se-oriented DCs are weakened, with bright spots appearing only around Se atoms due to the distance sensitivity of STM. Accordingly, STM images for Ge- and Se-oriented DCs show characteristic low-density voids and bright Se–Se bonds in the center as indicated by arrows, respectively. A similar weakening of current intensities is also observed in 60° GB-4, especially for negative bias in the range of [−0.15, 0] eV, while intensities increase slightly when positive bias in the range of [0, 0.15] eV is applied, attributing to the defect states of Se atoms around 0.12 eV near Γ point. These simulated STM images further illustrate that the metallicity in these systems is largely contributed from bulk atoms rather than DCs, induced by the resonance between bulk and defect states.

Differently, 60° GB-8 and GB-10 with horizontal Ge–Ge bonds show enhanced current intensities around Se atoms along GBs under both positive and negative biases. When GB-10 is under negative bias in the range of [−0.2, 0] eV, the characteristic Ge–Ge bonds also emerge, as indicated by arrows. These electron and hole tunneling current features at GBs around the Fermi level provide strong support for their experimental identification. GBs with intriguing properties may find potential applications if engineered purposefully.

CONCLUSIONS

In conclusion, by using first-principles calculations combined with topological principles for dislocation theory, we explore structures and thermodynamics of DCs and GBs in monolayer γ-GeSe, as well as their consequences on electronic structures. Structural and energy analysis show that DCs in pentagon-heptagon 5|7 shape are generally more favored than those in square-hexagon 4|6 and hexagon-octagon 6|8 rings. DCs with a Ge atom in the center of smaller pentagons and more hetero-elemental bonds exhibit lower energies than those with a Ge atom in larger heptagons. The GBs assembled by an array of low-energy DCs could undergo significant structural relaxations, depending on the symmetry between two mutually tilted crystalline domains. Different from 1H-MoS_2 or h-BN, 21.8° GBs in γ-GeSe with closely distributed dislocations generally induce a strong resonance effect between dislocation and bulk states, giving rise to metallic features. While 60° GBs can exhibit both semiconducting behaviors with greatly reduced band gap and resonance-induced metallicity depending on different structures. All these GBs possess distinct STM features. Our findings could also be feasibly generalized to other group IV MX and many other 2D materials in 1T phase with ABC stacking. Considering the versatile properties of topological defects in γ-phase group IV MX, careful attention should be paid to the synthesis and engineering for their potential applications.

Received 9 June 2022; accepted 4 August 2022; published online 4 November 2022

1 Castro Neto AH, Guinea F, Peres NMR, *et al.* The electronic properties of graphene. Rev Mod Phys, 2009, 81: 109–162
2 Fiori G, Bonaccorso F, Iannaccone G, *et al.* Electronics based on two-dimensional materials. Nat Nanotech, 2014, 9: 768–779
3 Wang QH, Kalantar-Zadeh K, Kis A, *et al.* Electronics and optoelectronics of two-dimensional transition metal dichalcogenides. Nat Nanotech, 2012, 7: 699–712
4 Tan CL, Cao XH, Wu XJ, *et al.* Recent advances in ultrathin two-dimensional nanomaterials. Chem Rev, 2017, 117: 6225–6331
5 Deng D, Novoselov KS, Fu Q, *et al.* Catalysis with two-dimensional materials and their heterostructures. Nat Nanotech, 2016, 11: 218–230
6 Anasori B, Lukatskaya MR, Gogotsi Y. 2D metal carbides and nitrides (MXenes) for energy storage. Nat Rev Mater, 2017, 2: 16098
7 Ma S, Cai M, Cheng T, *et al.* Two-dimensional organic-inorganic hybrid perovskite: from material properties to device applications. Sci China Mater, 2018, 61: 1257–1277
8 Hou H, Zeng X, Zhang X. 2D/2D heterostructured photocatalyst: Rational design for energy and environmental applications. Sci China Mater, 2020, 63: 2119–2152
9 Zhao LD, Lo SH, Zhang Y, *et al.* Ultralow thermal conductivity and high thermoelectric figure of merit in SnSe crystals. Nature, 2014, 508: 373–377
10 Fei R, Li W, Li J, *et al.* Giant piezoelectricity of monolayer group IV monochalcogenides: SnSe, SnS, GeSe, and GeS. Appl Phys Lett, 2015, 107: 173104
11 Zhang S, Liu S, Huang S, *et al.* Structural and electronic properties of atomically thin germanium selenide polymorphs. Sci China Mater, 2015, 58: 929–935
12 Wu M, Zeng XC. Intrinsic ferroelasticity and/or multiferroicity in two-dimensional phosphorene and phosphorene analogues. Nano Lett, 2016, 16: 3236–3241
13 Barraza-Lopez S, Fregoso BM, Villanova JW, *et al.* Colloquium: Physical properties of group-IV monochalcogenide monolayers. Rev Mod Phys, 2021, 93: 011001
14 Chang K, Liu J, Lin H, *et al.* Discovery of robust in-plane ferroelectricity in atomic-thick SnTe. Science, 2016, 353: 274–278
15 Fei R, Kang W, Yang L. Ferroelectricity and phase transitions in monolayer group-IV monochalcogenides. Phys Rev Lett, 2016, 117: 097601
16 Haleoot R, Paillard C, Kaloni TP, *et al.* Photostrictive two-dimensional materials in the monochalcogenide family. Phys Rev Lett, 2017, 118: 227401
17 He Y, Tang P, Hu Z, *et al.* Engineering grain boundaries at the 2D limit for the hydrogen evolution reaction. Nat Commun, 2020, 11: 57
18 Ji Y, Yang M, Dong H, *et al.* Two-dimensional germanium monochalcogenide photocatalyst for water splitting under ultraviolet, visible to near-infrared light. Nanoscale, 2017, 9: 8608–8615
19 Kim J, Kim KW, Shin D, *et al.* Prediction of ferroelectricity-driven Berry curvature enabling charge- and spin-controllable photocurrent in tin telluride monolayers. Nat Commun, 2019, 10: 3965
20 Zhu Z, Tománek D. Semiconducting layered blue phosphorus: A computational study. Phys Rev Lett, 2014, 112: 176802
21 Wang H, Qian X. Two-dimensional multiferroics in monolayer group IV monochalcogenides. 2D Mater, 2017, 4: 015042
22 Kennes DM, Xian L, Claassen M, *et al.* One-dimensional flat bands in twisted bilayer germanium selenide. Nat Commun, 2020, 11: 1124
23 Tian XQ, Duan JY, Kiani M, *et al.* Hexagonal layered group IV–VI semiconductors and derivatives: Fresh blood of the 2D family. Nanoscale, 2020, 12: 13450–13459
24 Mu X, Pan Y, Zhou J. Pure bulk orbital and spin photocurrent in two-dimensional ferroelectric materials. npj Comput Mater, 2021, 7: 61
25 Xu B, Deng J, Ding X, *et al.* Van der Waals force-induced intralayer ferroelectric-to-antiferroelectric transition *via* interlayer sliding in bi-

layer group-IV monochalcogenides. npj Comput Mater, 2022, 8: 47
26 Luo N, Duan W, Yakobson BI, *et al.* Excitons and electron-hole liquid state in 2D γ-phase group-IV monochalcogenides. Adv Funct Mater, 2020, 30: 2000533
27 Kim H, Choi HJ. Quasiparticle band structures, spontaneous polarization, and spin-splitting in noncentrosymmetric few-layer and bulk γ-GeSe. J Mater Chem C, 2021, 9: 9683–9691
28 Lee S, Jung JE, Kim HG, *et al.* γ-GeSe: A new hexagonal polymorph from group IV–VI monochalcogenides. Nano Lett, 2021, 21: 4305–4313
29 Zou X, Liu Y, Yakobson BI. Predicting dislocations and grain boundaries in two-dimensional metal-disulfides from the first principles. Nano Lett, 2013, 13: 253–258
30 Yazyev OV, Chen YP. Polycrystalline graphene and other two-dimensional materials. Nat Nanotech, 2014, 9: 755–767
31 Najmaei S, Liu Z, Zhou W, *et al.* Vapour phase growth and grain boundary structure of molybdenum disulphide atomic layers. Nat Mater, 2013, 12: 754–759
32 Liu Y, Yakobson BI. Cones, pringles, and grain boundary landscapes in graphene topology. Nano Lett, 2010, 10: 2178–2183
33 Zhang Z, Zou X, Crespi VH, *et al.* Intrinsic magnetism of grain boundaries in two-dimensional metal dichalcogenides. ACS Nano, 2013, 7: 10475–10481
34 Zhou X, Zhang Z, Guo W. Dislocations as single photon sources in two-dimensional semiconductors. Nano Lett, 2020, 20: 4136–4143
35 Zhang JJ, Guan J, Dong S, *et al.* Room-temperature ferroelectricity in group-IV metal chalcogenide nanowires. J Am Chem Soc, 2019, 141: 15040–15045
36 Gao N, Guo Y, Zhou S, *et al.* Structures and magnetic properties of MoS_2 grain boundaries with antisite defects. J Phys Chem C, 2017, 121: 12261–12269
37 Guo Y, Zhou S, Zhang J, *et al.* Atomic structures and electronic properties of phosphorene grain boundaries. 2D Mater, 2016, 3: 025008
38 Gibertini M, Marzari N. Emergence of one-dimensional wires of free carriers in transition-metal-dichalcogenide nanostructures. Nano Lett, 2015, 15: 6229–6238
39 Zou X, Liu M, Shi Z, *et al.* Environment-controlled dislocation migration and superplasticity in monolayer MoS_2. Nano Lett, 2015, 15: 3495–3500
40 Kresse G, Joubert D. From ultrasoft pseudopotentials to the projector augmented-wave method. Phys Rev B, 1999, 59: 1758–1775
41 Kresse G, Furthmüller J. Efficient iterative schemes for *ab initio* total-energy calculations using a plane-wave basis set. Phys Rev B, 1996, 54: 11169–11186
42 Perdew JP, Burke K, Ernzerhof M. Generalized gradient approximation made simple. Phys Rev Lett, 1996, 77: 3865–3868
43 Hammer B, Hansen LB, Nørskov JK. Improved adsorption energetics within density-functional theory using revised Perdew-Burke-Ernzerhof functionals. Phys Rev B, 1999, 59: 7413–7421
44 Tersoff J, Hamann DR. Theory of the scanning tunneling microscope. Phys Rev B, 1985, 31: 805–813
45 Momma K, Izumi F. *VESTA3* for three-dimensional visualization of crystal, volumetric and morphology data. J Appl Crystlogr, 2011, 44: 1272–1276
46 Liu YY, Zou XL, Yakobson BI. Dislocations and grain boundaries in two-dimensional boron nitride. ACS Nano, 2012, 6: 7053–7058
47 Li WX, Stampfl C, Scheffler M. Insights into the function of silver as an oxidation catalyst by *ab initio* atomistic thermodynamics. Phys Rev B, 2003, 68: 165412
48 Duan X, Warschkow O, Soon A, *et al.* Density functional study of oxygen on Cu(100) and Cu(110) surfaces. Phys Rev B, 2010, 81: 075430
49 Zou XL, Yakobson BI. An open canvas—2D materials with defects, disorder, and functionality. Acc Chem Res, 2015, 48: 73–80
50 Zou X, Yakobson BI. Metallic high-angle grain boundaries in monolayer polycrystalline WS_2. Small, 2015, 11: 4503–4507
51 Yazyev OV, Louie SG. Topological defects in graphene: Dislocations and grain boundaries. Phys Rev B, 2010, 81: 195420
52 Ma YJ, Kolekar S, Diaz HC, *et al.* Metallic twin grain boundaries embedded in $MoSe_2$ monolayers grown by molecular beam epitaxy. ACS Nano, 2017, 11: 5130–5139
53 Ma YJ, Diaz HC, Avila J, *et al.* Angle resolved photoemission spectroscopy reveals spin charge separation in metallic $MoSe_2$ grain boundary. Nat Commun, 2017, 8: 14231

Acknowledgements This work was supported by the National Natural Science Foundation of China (11974197 and 51920105002), Guangdong Innovative and Entrepreneurial Research Team Program (2017ZT07C341), and the Bureau of Industry and Information Technology of Shenzhen for the 2017 Graphene Manufacturing Innovation Center Project (201901171523).

Author contributions Zou X conceptualized this work. Zeng S conducted the first-principles calculations. Zeng S and Zou X contributed to the discussion and the writing of the manuscript, with approval to the final version of the manuscript.

Conflict of interest The authors declare that they have no conflict of interest.

Supplementary Information Supporting data are available in the online version of the paper.

Shengfeng Zeng is a PhD candidate in Prof. Xiaolong Zou's group at Tsinghua Berkeley Shenzhen Institute, Tsinghua Shenzhen International Graduate School. He obtained his BSc degree in materials science and engineering from the University of Science and Technology Beijing in 2020. His research mainly focuses on the topological defects and the optical behaviors of defects in 2D materials.

Xiaolong Zou received his BSc degree in physics from Tsinghua University in 2006 and PhD degree in condensed matter physics from Tsinghua University in Prof. Wenhui Duan' group in 2011. Then he worked as a postdoctoral fellow at Rice University in Prof. Boris I Yakobson's group from 2011 to 2016. He is currently an associate professor at Shenzhen Geim Graphene Center and Tsinghua Shenzhen International Graduate School, focusing on theoretical calculations on topological defects, magnetism and optical behaviors in 2D materials.

单层半导体性γ相第四主族单硫化合物中的拓扑缺陷及其诱导的金属性

曾圣锋, 邹小龙*

摘要 γ相第四主族单硫化合物(γ-MX)是理论预测出的一种全新的具有半导体特性的稳定结构. 最近, 人们通过化学气相沉积法成功合成了相关材料, 但样品却表现出金属性. 生长过程引入的拓扑缺陷无处不在, 可能会对材料电子行为带来重要影响. 但是, 关于这些拓扑缺陷的结构和性质的研究仍未开展. 以γ相GeSe为例, 我们通过第一性原理计算系统研究了其位错核和晶界的结构、热力学和电子性质. 结果发现, 不同的原子排布方式可以形成多样的衍生位错核. 基于最低能量的位错核, 我们研究了晶界结构随着倾斜角的变化, 并特别构建了全部可能的60°孪生晶界, 发现它们具有独特的六边形结构或Ge–Ge键. 进一步地, 针对能量最低的21.8°和60°晶界的电子结构分析发现, 大多数晶界体态和缺陷态之间具有共振作用, 这使得体系表现出金属性质; 而某些结构则仍表现半导体性, 但带隙显著减小. 这些电子性质在其他γ-MX中也普遍存在. 不同晶界的扫描隧道显微镜图像展现出特征性图案, 可以作为表征它们的手段. 我们的结果表明, 应对γ-MX中具有多样性质的拓扑缺陷进行有目的的设计以促进其潜在应用.

